

Sub-Pixel Mapping Based on a MAP Model With Multiple Shifted Hyperspectral Imagery

Xiong Xu, Yanfei Zhong, *Member, IEEE*, Liangpei Zhang, *Senior Member, IEEE*, and Hongyan Zhang

Abstract—Sub-pixel mapping is technique used to obtain the spatial distribution of different classes at the sub-pixel scale by transforming fraction images to a classification map with a higher resolution. Traditional sub-pixel mapping algorithms only utilize a low-resolution image, the information of which is not enough to obtain a high-resolution land-cover map. The accuracy of sub-pixel mapping can be improved by incorporating auxiliary datasets, such as multiple shifted images in the same area, to provide more sub-pixel land-cover information. In this paper, a sub-pixel mapping framework based on a maximum a posteriori (MAP) model is proposed to utilize the complementary information of multiple shifted images. In the proposed framework, the sub-pixel mapping problem is transformed to a regularization problem, and the MAP model is used to regularize the sub-pixel mapping problem to be well-posed by adding some prior information, such as a Laplacian model. The proposed algorithm was compared with a traditional sub-pixel mapping algorithm based on a single image, and another multiple shifted images based sub-pixel mapping method, using both synthetic and real hyperspectral images. Experimental results demonstrated that the proposed approach outperforms the traditional sub-pixel mapping algorithms, and hence provides an effective option to improve the accuracy of sub-pixel mapping for hyperspectral imagery.

Index Terms—Hyperspectral image, MAP, multiple shifted images, resolution enhancement, sub-pixel mapping, super-resolution mapping.

I. INTRODUCTION

HARD classification, an important technique in image processing, assigns every pixel to a single class; however, it is inaccurate in hyperspectral images with a coarse resolution, due to the mixed pixel problem [1]. Spectral unmixing techniques are introduced to obtain the abundance of each class in the mixed pixel by yielding a number of fraction images equal to the number of land-cover classes [2]. However, the sub-pixel spatial attribution of the different classes in a pixel cannot be obtained by spectral unmixing, and the sub-pixel information may be lost. To solve the problem, sub-pixel mapping was introduced by Atkinson [3], which divides a pixel into sub-pixels

and assigns each new smaller sub-pixel to a land-cover class in order to obtain a hard classification map with higher resolution.

Many sub-pixel mapping algorithms have been proposed based on spatial dependence [3], which refers to the tendency for spatially proximate observations of a given property to be more alike than more distant observations. For example, Tatem *et al.* built an energy function and applied a Hopfield neural network [4]–[7] to solve the problem. Another artificial neural network, the BP (back-propagation) neural network, has been used to obtain the sub-pixel mapping result [8], [9]. Verhoeve *et al.* [10] transformed the issue of sub-pixel mapping to an optimization problem, using a linear optimization technique. To satisfy the demand of spatial dependence, a simple but effective method based on sub-pixel/pixel spatial attraction models was proposed by Mertens *et al.* [11]. Atkinson *et al.* presented a pixel swapping algorithm [12] to exchange sub-pixels to obtain an optimal result. More recently, genetic algorithms [13], artificial immune systems [14], Markov random fields [15], [16], and multi-layer perceptron neural network [17] have been utilized for sub-pixel mapping.

Most of the traditional methods only utilize the soft-classified proportion of the data of a single image at the pixel level, and are based on the spatial dependence assumption [18]. In fact, sub-pixel mapping can be formulated as an inverse problem that reconstructs a fine spatial resolution map of land-cover class labels from a set of class fractions provided by a low-resolution image [19]. Consequently, sub-pixel mapping is also an ill-posed problem that transforms a low-resolution fraction image to a high-resolution classification map, and traditional methods based on single images have a limit to the detail and accuracy of the resulting thematic map. Therefore, additional supplementary datasets should be used. Many types of auxiliary datasets are available, such as light detection and ranging (LIDAR) [20], fused image [18], and panchromatic imagery [21]. However, these suitable datasets are often hard to acquire. Another possible auxiliary dataset comprises sub-pixel shifted images generated by camera movements in the same area of land surface, which may be easily obtained from multi-temporal or multi-angle images with a sub-pixel shift. Multiple shifted fraction maps derived from these images can therefore provide additional land-cover information at the sub-pixel scale, which can, theoretically, be used to improve the accuracy of super-resolution mapping [19].

In this paper, to utilize these multiple shifted fraction images synchronously to improve the sub-pixel mapping accuracy, a sub-pixel mapping framework based on a maximum a posteriori (MAP) model with multiple shifted hyperspectral images, namely MMSSM, is proposed. In the proposed frame-

Manuscript received July 19, 2012; revised September 13, 2012; accepted October 23, 2012. Date of publication December 10, 2012; date of current version May 13, 2013. This work was supported in part by National Basic Research Program of China (973 Program) under Grant 2011CB707105, by the National Natural Science Foundation of China under Grant 40901213 and Grant 61201342, and by A Foundation for the Author of National Excellent Doctoral Dissertation of P.R. China (FANEDD) under Grant 201052.

The authors are with the State Key Laboratory of Information Engineering in Surveying, Mapping and Remote Sensing, Wuhan University, Wuhan 430079, China (e-mail: zhongyanfei@whu.edu.cn).

Color versions of one or more of the figures in this paper are available online at <http://ieeexplore.ieee.org>.

Digital Object Identifier 10.1109/JSTARS.2012.2227246

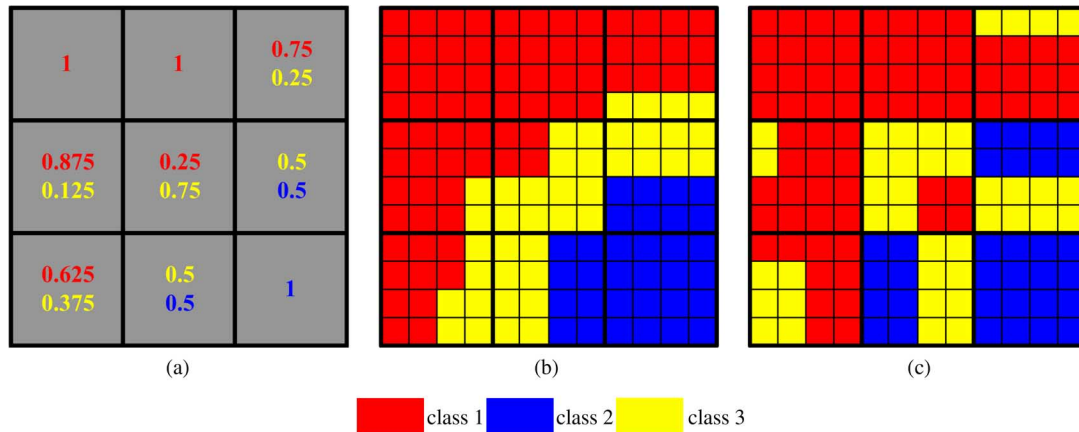


Fig. 1. Image of 3×3 coarse pixels and the possible distributions (scale = 4, 3 classes). (a) Fraction image. (b) Possible distribution 1. (c) Possible distribution 2.

work, the MAP model, due to the advantages of expansibility and the ease of adding prior information, is utilized to integrate the complementary information in multiple images with a sub-pixel shift. The MAP model has the ability to regularize the ill-posed problem and has also been successfully used in the field of multiple-frame super-resolution (SR) reconstruction to produce a high-resolution (HR) image from a sequence of low-resolution (LR) images of the same scene [22]–[26]. In MMSSM, the MAP method, as a basic framework, is utilized to reconstruct a classification map with higher resolution from the multiple fraction images with a lower resolution. In the MAP framework, three prior models (Laplacian [27], total variation [TV] [28], and bilateral total variation [BTV] [29]), are used to regularize the sub-pixel mapping problem, in order to improve the performance of MMSSM for sub-pixel mapping. The proposed method was tested using three synthetic hyperspectral images and one real hyperspectral image, and the experimental results demonstrated that the proposed approach obtains a better result by incorporating the information from multiple images.

The rest of this paper is organized as follows: Section II gives a detailed description of the sub-pixel mapping problem. The proposed sub-pixel mapping framework based on a MAP model with multiple shifted hyperspectral images is described in detail in Section III. Section IV gives the experimental results and analysis using different images. The conclusion is drawn in Section V.

II. THE SUB-PIXEL MAPPING PROBLEM

A. The Sub-Pixel Mapping Problem

The key issue in sub-pixel mapping is how to determine an optimal sub-pixel distribution of each class in a pixel. Spatial dependence, as proposed by Atkinson in 1997, inspired from Tobler's first law [30], is the universal criterion, which refers to the tendency for spatially proximate observations of a given property to be more alike than more distant observations [3]. To implement a sub-pixel mapping algorithm, fraction images, as the input, should be obtained by means of spectral unmixing. An original coarse pixel in the fraction image is divided into $S \times S$ sub-pixels, where S represents the scale factor of the

sub-pixel mapping, and the number of sub-pixels for each land-cover class can be calculated by the abundance. Fig. 1 shows a sub-pixel mapping example with three classes. As shown in Fig. 1(a), a coarse pixel is divided into 16 (4×4) sub-pixels, with the assumption that the scale fraction S is 4, and 0.5 in the fraction image in red, which means that 8 (16×0.5) sub-pixels belong to land-cover class 1. Fig. 1(b) and (c) describes two possible distributions of sub-pixels, where the former is superior to the latter, with higher spatial dependence.

B. The Sub-Pixel Mapping Problem Based on Multiple Shifted Images

The drawback of traditional sub-pixel mapping methods is lacking enough information. This is because the sub-pixel mapping problem can be formulated as an ill-posed problem, whose number of solutions is not unique, by utilizing fraction images derived from a single hyperspectral image. Sub-pixel mapping with multiple shifted images is a feasible way to solve this problem by introducing more sub-pixel information. The basic idea is to combine several low-resolution fraction (LRF) images from the same scene to produce one high-resolution fraction image. Although these LRF images are derived from the same scene, they are not identical to each other, because of the camera movements. Therefore, the different information contained in each LRF image can be fused to produce a high-resolution classification (HRC) image. Fig. 2 illustrates a simple example with two classes, to explain the process of how to integrate multiple shifted LRF images to obtain a HRC image. As shown in Fig. 2, in pixel P1, the fraction of class A is 0.25, and the scale factor S is 4, in which 4 ($4 \times 4 \times 0.25$) sub-pixels belong to class A. Given another pixel P2 from another image, which has a sub-pixel shift (the fraction of class A is 1, $dx = 0.5$ pixel, $dy = 0.5$ pixel) with pixel P1, as shown in Fig. 2(b), the position of the sub-pixels which belong to class A can be determined, as all the sub-pixels in pixel P2 belong to class A, because P2 is the pure pixel, which belonged to A. According to the above process, based on multiple shifted LRF images, a more accurate sub-pixel mapping result can be obtained.

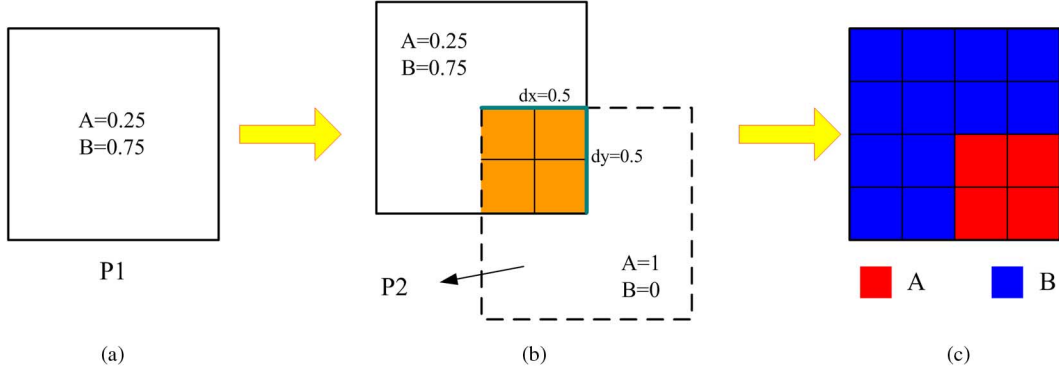


Fig. 2. The sub-pixel mapping process using multiple shifted images. (a) A mixed pixel P1 with two different land-cover classes. (b) Another pixel P2, which has a sub-pixel shift with P1. (c) The sub-pixel mapping result using two multiple shifted images.

III. SUB-PIXEL MAPPING FRAMEWORK BASED ON A MAXIMUM A POSTERIORI (MAP) MODEL WITH MULTIPLE SHIFTED HYPERSPECTRAL IMAGES

To solve the sub-pixel mapping problem with multiple shifted images, a sub-pixel mapping framework based on a maximum a posteriori (MAP) model with multiple shifted hyperspectral images, namely MMSSM, is proposed to convert the LRF image sequence to a HRC map. In this framework, the sub-pixel mapping problem is first transformed to a regularization problem, and the MAP model is then used to regularize the sub-pixel mapping problem to be well-posed by adding some prior information, which, in this paper, comprises Laplacian, TV and BTM prior models.

A. Problem Formulation

In the proposed framework, the sub-pixel mapping problem with multiple shifted images needs to be defined as follows. Let the underlying HRC image be denoted in the vector form by $\mathbf{y} = f(\mathbf{y}^1, \mathbf{y}^2 \cdots \mathbf{y}^C)$, where C is the number of land-cover classes. In other words, C is the band number of the original LRF image, and \mathbf{y}^c is the high-resolution MAP (HRM) image for class $c \in [1, C]$. $f(\cdot)$ is the integration function used to transform the HRM images for all classes to a HRC map. Letting (m, n) denote the height and width of the LRF images, (M, N) is the height and width of the HR image, and S represents the scale factor. The LRF image can be represented as $\mathbf{g}_k^c = [g_{k,1}^c, g_{k,2}^c, \dots, g_{k,m*n}^c]^T$, where $k = 1, 2, \dots, K$, with K being the number of LRF images. Then the mapping model can be represented as:

$$\mathbf{g}_k^c = \mathbf{D}\mathbf{M}_k\mathbf{y}^c + \mathbf{n}_k^c \quad (1)$$

where \mathbf{M}_k is the warp matrix with the size of $MN \times MN$, \mathbf{D} is a $mn \times MN$ downsampling matrix, and \mathbf{n}_k^c represents the $mn \times 1$ noise vector for class c . Generally, the downsampling matrix \mathbf{D} and the warp matrix \mathbf{M}_k are assumed to remain the same between the LRF images.

Referring to the form of (1), the whole mapping model for all the LRF images can be represented as:

$$\mathbf{g}^c = \mathbf{D}\mathbf{M}\mathbf{y}^c + \mathbf{n}^c \quad (2)$$

where $\mathbf{g}^c = [\mathbf{g}_1^c, \mathbf{g}_2^c \cdots \mathbf{g}_K^c]^T$, $\mathbf{M} = [\mathbf{M}_1, \mathbf{M}_2 \cdots \mathbf{M}_K]^T$, $\mathbf{n}^c = [\mathbf{n}_1, \mathbf{n}_2 \cdots \mathbf{n}_K]^T$.

In this paper, a MAP strategy is used to regularize the sub-pixel mapping problem to be well-posed by adding some prior information. Based on the mapping model of (2), the MAP approach seeks the $\hat{\mathbf{y}}_{MAP}^c$ to estimate \mathbf{y}^c , for which the a posteriori probability $\Pr(\mathbf{y}^c|\mathbf{g}^c)$ is a maximum [31], given the LRF images \mathbf{g}^c as (3):

$$\hat{\mathbf{y}}_{MAP}^c = \arg \max \{ \Pr(\mathbf{y}^c|\mathbf{g}^c) \} \quad (3)$$

Applying Bayes' rule, (3) becomes:

$$\hat{\mathbf{y}}_{MAP}^c = \arg \max \left\{ \frac{\Pr(\mathbf{g}^c|\mathbf{y}^c) \Pr(\mathbf{y}^c)}{\Pr(\mathbf{g}^c)} \right\} \quad (4)$$

Since $\Pr(\mathbf{g}^c)$ can be considered as a constant and can be eliminated in the optimization of (4), (4) can be rewritten as:

$$\hat{\mathbf{y}}_{MAP}^c = \arg \max \{ \Pr(\mathbf{g}^c|\mathbf{y}^c) \Pr(\mathbf{y}^c) \} \quad (5)$$

Assuming the LRF images are independent, we can obtain:

$$\hat{\mathbf{y}}_{MAP}^c = \arg \max \left\{ \prod_k \Pr(\mathbf{g}_k^c|\mathbf{y}^c) \Pr(\mathbf{y}^c) \right\} \quad (6)$$

Using the monotonic logarithm function, (6) can be expressed as:

$$\hat{\mathbf{y}}_{MAP}^c = \arg \max \left\{ \sum_{k=1}^K \log \Pr(\mathbf{g}_k^c|\mathbf{y}^c) + \log \Pr(\mathbf{y}^c) \right\} \quad (7)$$

where $\Pr(\mathbf{g}_k^c|\mathbf{y}^c)$ is the likelihood distribution of the LRF images, and $\Pr(\mathbf{y}^c)$ is the prior distribution of the image \mathbf{y}^c .

Assuming the noise is zero-mean white Gaussian noise with the same variance, $\Pr(\mathbf{g}_k^c|\mathbf{y}^c)$ can be represented as:

$$\Pr(\mathbf{g}_k^c|\mathbf{y}^c) = \frac{1}{\rho_1} \exp \left(-\frac{\|\mathbf{g}_k^c - \mathbf{D}\mathbf{M}_k\mathbf{y}^c\|^2}{2\sigma^2} \right) \quad (8)$$

where ρ_1 is a constant and σ^2 is the variance. The prior $\Pr(\mathbf{y}^c)$ is thought to be the Gibbs form:

$$\Pr(\mathbf{y}^c) = \frac{1}{\rho_2} \exp \left(-\frac{1}{\beta} U(\mathbf{y}^c) \right) \quad (9)$$

where ρ_2 is a constant, β is a control parameter, and $U(\mathbf{y}^c)$ is the energy function. Substituting (8) and (9) in (7), the maximization of this posterior probability distribution can be written as the following regularization problem:

$$\hat{\mathbf{y}}_{MAP}^c = \arg \min \left\{ \sum_{k=1}^K \|\mathbf{g}_k^c - \mathbf{D}\mathbf{M}_k \mathbf{y}^c\|^2 + \lambda U(\mathbf{y}^c) \right\} \quad (10)$$

where $\lambda = 2\sigma^2/\beta$. The first term $\|\mathbf{g}_k^c - \mathbf{D}\mathbf{M}_k \mathbf{y}^c\|^2$ is the data fidelity term. $U(\mathbf{y}^c)$ acts as the prior term, and λ is the regularization parameter which controls the trade-off between the data fidelity and prior item.

B. Model Solution

After defining the problem, MMSSM solves the model according to three steps:

Step 1) Determination of the motion matrix and prior model.

The estimation of motion matrix \mathbf{M} in (10) plays an important role in the process of a MAP model solution. After a LRF image is selected as the reference from the LRF image sequences, the sub-pixel shift between the reference LRF image and the other LRF images can be estimated by the parametric model which was used in [32], with the assumption that the motion of LRF images is a globally translational motion, and the motions of all points can often be modeled by a parametric model.

The prior model $U(\mathbf{y}^c)$ is also critical in the proposed method; it controls the perturbation of the solution, solves the ill-posed problem for the proposed model, and guarantees a stable HR estimation [33]. In past decades, many prior models have been proposed, such as the Gaussian Markov random fields (GMRF) model [34], the Huber-MRF model [24], the weighted-MRF model [32], the Laplacian model [27], the TV model [28], the BTV model [29], and sparse directional regularization [35]. In this paper, the prior model is assumed to be the same for all classes, and three prior models (Laplacian, TV, and BTV) are applied to test the performance of the MAP model in sub-pixel mapping.

1) Laplacian prior model

The Laplacian prior is a 2-D Laplacian matrix which denotes the high-pass operation with the constraint that the solution is smooth. The model is represented as [27]:

$$U(\mathbf{y}^c) = \|\mathbf{Q}\mathbf{y}^c\|_2^2 \quad (11)$$

where \mathbf{Q} is the Laplacian matrix.

2) TV prior model.

The TV prior is used to effectively preserve the edge and detailed information in images, and it can be represented as [28]:

$$U(\mathbf{y}^c) = \sum_i \sum_j \sqrt{|\nabla y_h^c|^2 + |\nabla y_v^c|^2} \quad (12)$$

where ∇y_h^c and ∇y_v^c are linear operators denoting the horizontal and vertical first-order differences. For pixel $[i, j]$, which is located in row i and column j in image \mathbf{y}^c , ∇y_h^c and ∇y_v^c can be computed as $\nabla y_h^c = y^c[i+1, j] - y^c[i, j]$, $\nabla y_v^c = y^c[i, j+1] - y^c[i, j]$.

3) BTV prior model.

The BTV prior is derived from TV by adding a bilateral filter. It has the advantages of edge preservation and being computationally cheap to implement. The l_1 form of TV can be regarded as a special case of the BTV model. Generally, the expression of BTV can be written as [29]:

$$U(\mathbf{y}^c) = \sum_{l=-P}^P \sum_{m=0}^P \alpha^{|m|+|l|} \|\mathbf{y}^c - \mathbf{S}_h^l \mathbf{S}_v^m \mathbf{y}^c\|_1 \quad (13)$$

where matrices \mathbf{S}_h^l and \mathbf{S}_v^m shift \mathbf{y}^c by l and m pixels in the horizontal and vertical directions, respectively. The scalar weight α , $0 < \alpha < 1$, is applied to give a spatially decaying effect to the summation of the regularization terms [29].

Step 2) Upsampling of the high-resolution MAP (HRM) result for every class.

Once the motion matrix and prior model are determined, the desired HRM image can be updated by minimizing the following cost function:

$$E(\mathbf{y}^c) = \sum_{k=1}^K \|\mathbf{g}_k^c - \mathbf{D}\mathbf{M}_k \mathbf{y}^c\|^2 + \lambda U(\mathbf{y}^c) \quad (14)$$

The gradient descent [36] method is utilized to minimize the cost function. Differentiating (14) with respect to \mathbf{y}^c , and setting the result equal to zero, we have:

$$\nabla E(\mathbf{y}^c) = -2 \sum_{k=1}^K \mathbf{M}_k^T \mathbf{D} (\mathbf{g}_k^c - \mathbf{D}\mathbf{M}_k \mathbf{y}^c) + \lambda \nabla U(\mathbf{y}^c) \quad (15)$$

where $\nabla U(\mathbf{y}^c)$ can be calculated as (16)–(18) for the Laplacian, TV and BTV priors, respectively:

$$\text{Lap} : U(\mathbf{y}^c) = \|\mathbf{Q}\mathbf{y}^c\|_2^2 \Rightarrow \nabla U(\mathbf{y}^c) = 2\mathbf{Q}^T \mathbf{Q}\mathbf{y}^c \quad (16)$$

$$\begin{aligned} \text{TV} : U(\mathbf{y}^c) &= \sum_i \sum_j \sqrt{|\nabla y_h^c|^2 + |\nabla y_v^c|^2} \\ &\Rightarrow \nabla U(\mathbf{y}^c) = \sum_i \sum_j \nabla \left(\frac{[\nabla y_h^c \quad \nabla y_v^c]^T}{\sqrt{|\nabla y_h^c|^2 + |\nabla y_v^c|^2 + \beta}} \right) \end{aligned} \quad (17)$$

$$\begin{aligned} \text{BTV} : U(\mathbf{y}^c) &= \sum_{l=-P}^P \sum_{m=0}^P \alpha^{|m|+|l|} \|\mathbf{y}^c - \mathbf{S}_h^l \mathbf{S}_v^m \mathbf{y}^c\|_1 \\ &\Rightarrow \nabla U(\mathbf{y}^c) = \sum_{l=-P}^P \sum_{m=0}^P \alpha^{|m|+|l|} [\mathbf{I} - \mathbf{S}_h^{-l} \mathbf{S}_v^{-m}] \\ &\quad \times \text{sign}(\mathbf{y}^c - \mathbf{S}_h^l \mathbf{S}_v^m \mathbf{y}^c) \end{aligned} \quad (18)$$

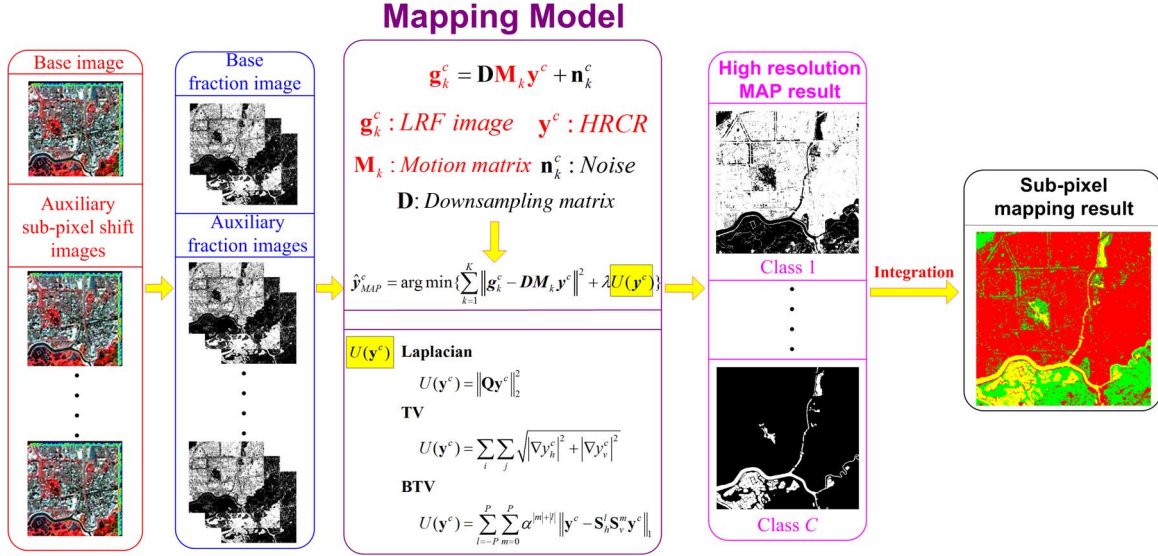


Fig. 3. The flowchart of MMSSM.

where $\nabla \cdot ()$ is the divergence operator, and β is a small positive parameter which ensures differentiability. S_h^{-l} and S_v^{-m} define the transposes of matrices S_h^l and S_v^m respectively and have a shifting effect in the opposite directions as S_h^l and S_v^m . Thus, the desired HRM image is solved by employing the successive approximations iteration:

$$\widehat{\mathbf{y}}_{n+1}^c = \widehat{\mathbf{y}}_n^c + \alpha_n^c \mathbf{r}_n^c \quad (19)$$

where

$$\mathbf{r}_n^c = 2 \sum_{k=1}^K \mathbf{M}_k^T \mathbf{D} (\mathbf{g}_k^c - \mathbf{D} \mathbf{M}_k \widehat{\mathbf{y}}_n^c) - \lambda \nabla U(\widehat{\mathbf{y}}_n^c) \quad (20)$$

and α_n^c represents the step size at the n th iteration.

Step 3) Integration of the HRM images to generate the HRC map.

All the MAP results \mathbf{y}^c for every class c should be integrated to obtain the HRC image \mathbf{y} . $S * S$ sub-pixels in \mathbf{y}^c , which correspond to a coarse pixel, should be normalized to $[0,1]$, and the class of sub-pixel will be z , with the condition that $y^z = \max\{y^c | c = 1, 2 \dots C\}$.

The flowchart of the proposed method is shown in Fig. 3.

IV. EXPERIMENTS AND ANALYSIS

In the experiments, three proposed algorithms based on Laplacian, TV, and BTV prior models in MMSSM, namely, MMSSM-L, MMSSM-TV, and MMSSM-BTV, were utilized to compare with traditional sub-pixel mapping methods with a single image (the spatial attraction model [SASM] [11]) and another multiple shifted images based method which utilizing Hopfield Neural Network (super-resolution mapping with multiple sub-pixel shifted images [SMMI] [19]), using both synthetic and real hyperspectral images. Traditional classification accuracy assessment was completed by the indices of percentage correctly classified (PCC), which is identical to

overall accuracy (OA), and the Kappa coefficient (Kappa). For the sub-pixel mapping problem, to better measure the capacity of different methods to handle mixed pixels, some other improved indices were used, specifically, PCC' and Kappa' [9]. Unlike the traditional indices, only mixed pixels are concerned in the calculation of PCC' and Kappa'. In the real hyperspectral image experiment, only PCC and Kappa were used because the results of the LRF images were not accurate, due to the limitation of the spectral unmixing techniques currently available.

A. Experiment 1-Synthetic Images

To simulate a series of LRF images with sub-pixel shifts, a HRC image was obtained by classifying a hyperspectral image first, then the HRC image was shifted at the pixel scale in the x and y directions, and the HRC image was degraded to simulate an LRF image by applying an averaging filter, given the resize factor. This procedure was performed many times, according to the number of images used for the proposed algorithm. In this way, the original classification map can be used as a reference image to evaluate the sub-pixel mapping methods, and it is possible to concentrate solely on errors introduced by the sub-pixel mapping process.

Three synthetic images were used in this experiment. One is a part of the Hyperspectral Digital Imagery Collection Experiment (HYDICE) airborne hyperspectral dataset from the Washington DC Mall. A total of 192 bands [37] were used, comprising 300 lines and 200 columns, as shown in Fig. 4(a). Fig. 4(b) shows the selected pixels which were used as the ground truth to evaluate the classification result, and Fig. 4(c) illustrates the reference image classified by the support vector machine (SVM) method, implemented by ENVI software [38], as the truth data. As the shift of the classification map was known, these degraded LRF images could be accurately registered at the sub-pixel scale, given the scale factor which was four. The number of LRF images in this experiment was five, and the shifts of the LRF images were $(-0.5, 0)$, $(0.5, 0)$, $(0, -0.5)$, $(0, 0.5)$, relative to the base LRF image. The observed

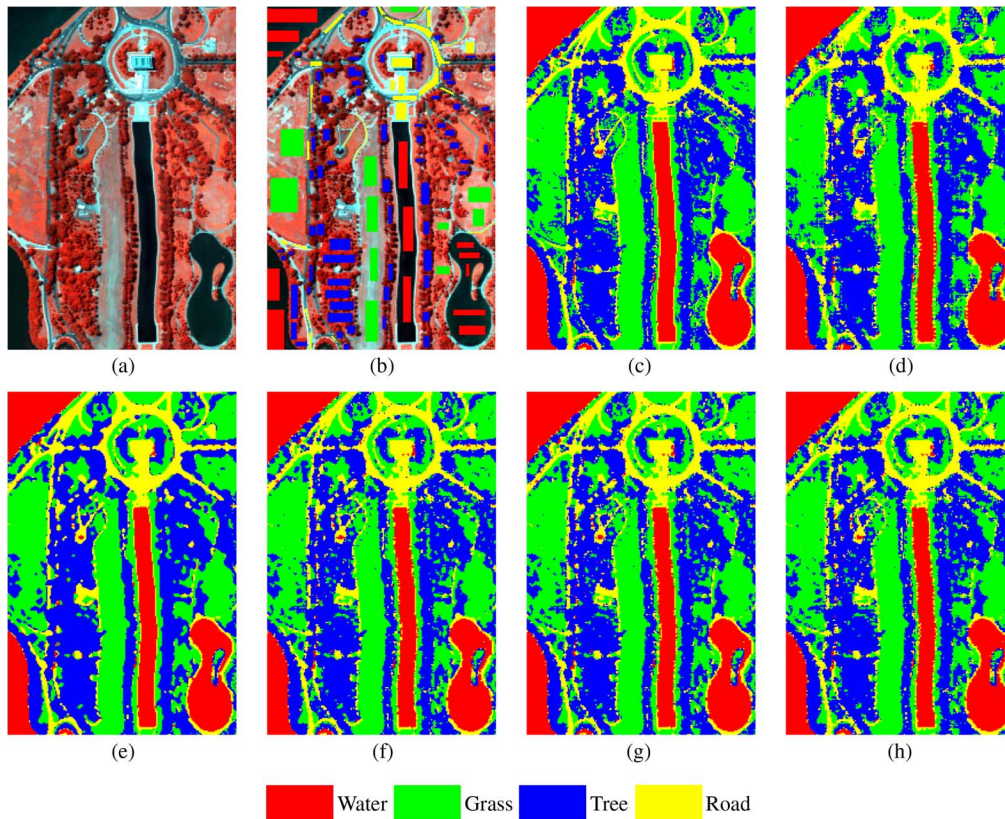


Fig. 4. The sub-pixel mapping results for the Washington DC dataset. (a) The original hyperspectral image. (b) The ground truth selected manually to evaluate the classification result. (c) The reference classification map. (d) SASM. (e) SMMI. (f) MMSSM-L. (g) MMSSM-TV. (h) MMSSM-BTV.

TABLE I
THE ACCURACY OF THE CLASSIFICATION METHOD FOR
THE WASHINGTON DC IMAGE

Methods	Class	Water	Grass	Tree	Road
SVM	Water	3206	0	0	0
	Grass	0	2685	20	116
	Tree	0	162	3030	1
	Road	0	0	5	1318
PCC = 97.12% Kappa = 0.961					

image was expected to fall into four classes: water, grass, tree and road. Fig. 4(d), (e) and (f)–(h) illustrates the sub-pixel mapping results using SASM, SMMI and the proposed methods, respectively.

To estimate the error introduced by the classification method, many pixels were manually selected as the ground truth, as Fig. 4(b) illustrates. In this paper, the reference classification map was obtained by classifying the original remotely sensed image with SVM, and the accuracy of SVM is shown in Table I. The results show that misclassification occurs between grass and tree, owing to the spectral proximity. It also occurs between grass and road, and these kinds of misclassification may occur in the following sub-pixel mapping experiments. However, this classification map can be used as a reference image for sub-pixel mapping, with a Kappa coefficient of 0.961.

Another image used is a part of a remote sensing image collected with an airborne imaging spectrometer (PHI) from the Xiaqiao test site. A total of 80 bands of the PHI image (160×160 pixels) were utilized, with a spectral range of 440–854 nm. The LRF image sequence was obtained as described for the Washington DC dataset. The scale factor was set as four, the number of LRF images was five and the shifts[0] of the LRF images were $(-0.5, 0)$, $(0.5, 0)$, $(0, -0.5)$, $(0, 0.5)$, relative to the base LRF image in this experiment. Fig. 5(a) shows the original PHI hyperspectral image cube; Fig. 5(b) shows the selected pixels which were used as the ground truth to evaluate the classification result; and Fig. 5(c) is the reference classification map obtained by SVM, in which four major land-cover classes can be distinguished: road, water, corn, and vegetable. Fig. 5(d), (e) and (f)–(h) illustrates the sub-pixel mapping results using SASM, SMMI and the proposed methods, respectively.

The classification accuracies are listed in Table II. As this image was not particularly complex, so that the distinct differences between classes can be observed, along with the impact of the selection of the ground truth, SVM can be seen to be highly accurate, and the result was considered to be suitable for the experiments with sub-pixel mapping.

The last image used was the AVIRIS data set. Seventeen land cover classes were considered for classification. The original image is composed of 136×136 pixels, and the ground truth data was used as the reference data. The LRF image sequence was obtained as described in the Washington DC dataset experiment. The scale factor was set as four, the number of LRF images was five and the shifts[0] of the LRF images were

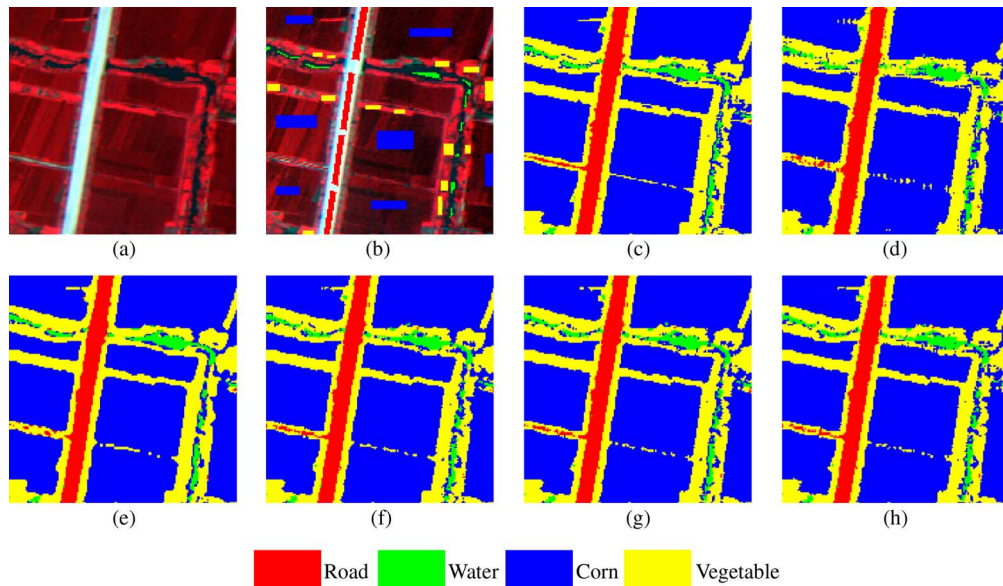


Fig. 5. The sub-pixel mapping results for the Xiaqiao dataset. (a) The original hyperspectral image. (b) The ground truth selected manually to evaluate the classification result. (c) The reference classification map. (d) SASM. (e) SMMI. (f) MMSSM-L. (g) MMSSM-TV. (h) MMSSM-BTV.

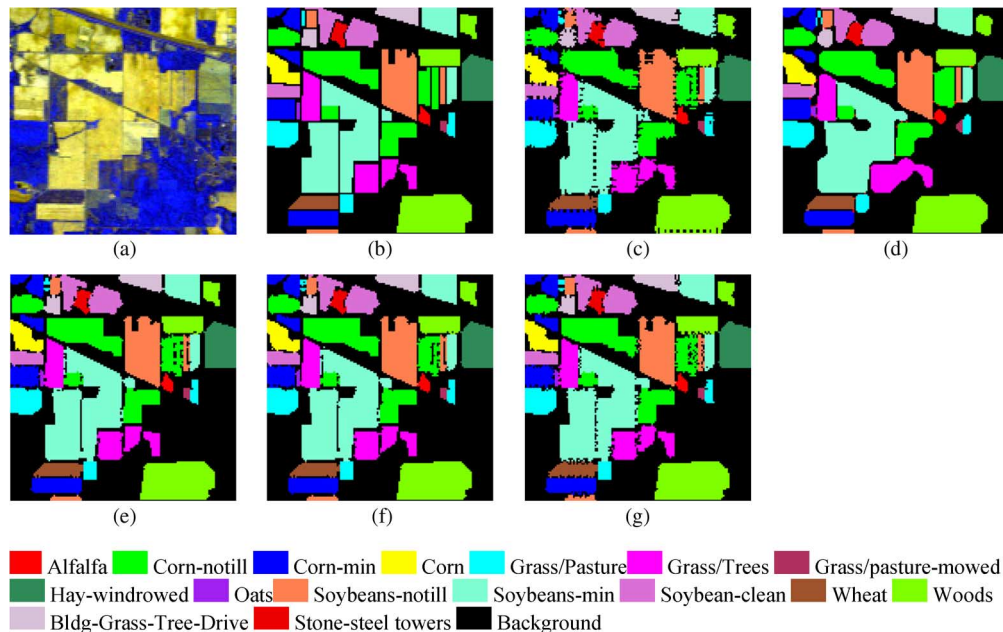


Fig. 6. The sub-pixel mapping results for the AVIRIS Indian Pines dataset. (a) The original hyperspectral image. (b) The ground truth data as the reference classification map. (c) SASM. (d) SMMI. (e) MMSSM-L. (f) MMSSM-TV. (g) MMSSM-BTV.

TABLE II
THE ACCURACY OF THE CLASSIFICATION METHOD FOR THE XIAQIAO IMAGE

Methods	Class	Road	Water	Corn	Vegetable
SVM	Road	701	0	0	0
	Water	0	154	0	0
	Corn	0	4	1260	7
	Vegetable	1	0	0	512
PCC = 99.54% Kappa = 0.993					

$(-0.5, 0)$, $(0.5, 0)$, $(0, -0.5)$, $(0, 0.5)$, relative to the base LRF image in this experiment. Fig. 6(a) shows the original AVIRIS

hyperspectral image cube; Fig. 6(b) shows the ground truth data in which 17 major land-cover classes can be distinguished. Fig. 6(c), (d) and (e)–(g) illustrate the sub-pixel mapping results using SASM, SMMI and three proposed methods, respectively.

As shown in Figs. 4–6, a visual comparison of the results suggests that the proposed method is successful in utilizing the complementary information of multiple images (which have sub-pixel shifts) to implement the task of sub-pixel mapping. In particular, some tiny features, such as the narrow path in the top left of the classification map for the Washington DC dataset, are not easily reconstructed using SASM, due to insufficient information. For the Xiaqiao image, the linear feature in the vegetable class can't be reconstructed well. For the AVIRIS image, some lines were over-smoothed in the result of SMMI. However, the proposed methods perform better by integrating

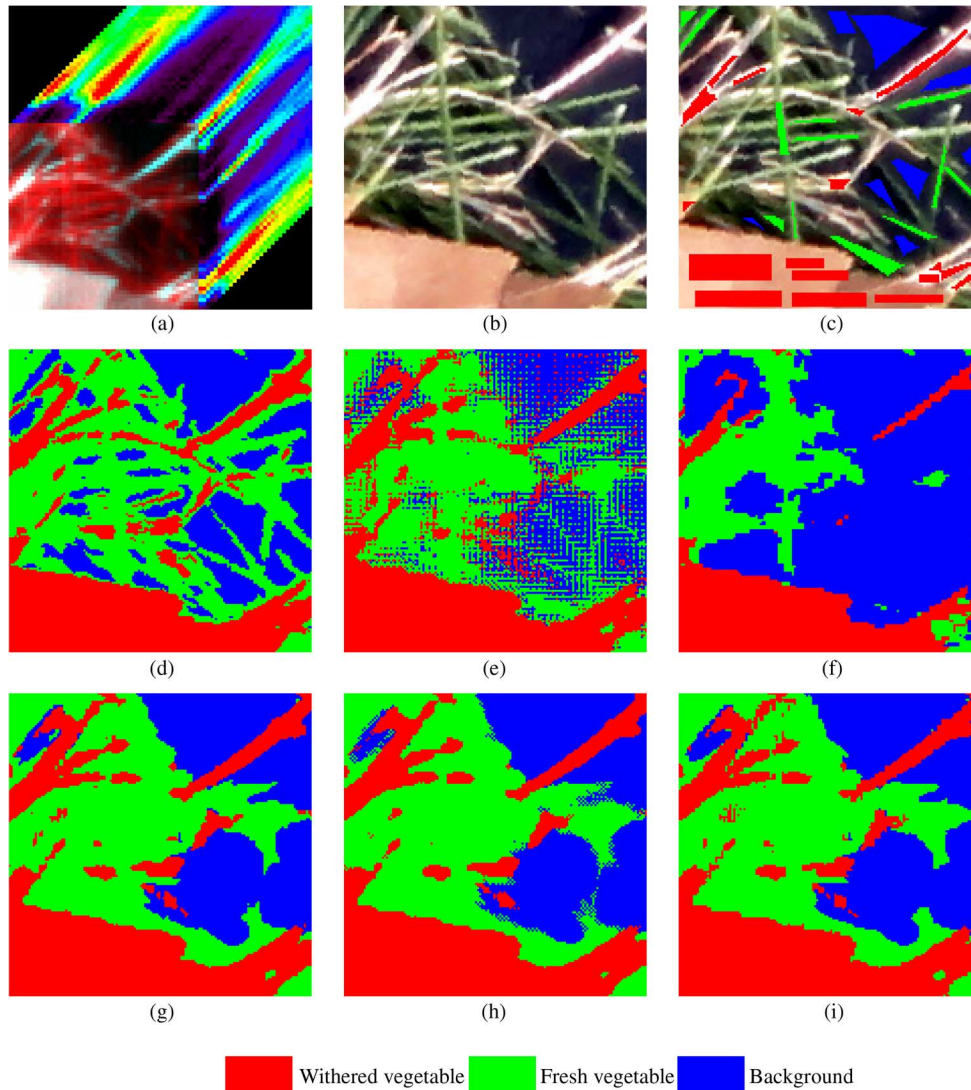


Fig. 7. The sub-pixel mapping results for the Nuance hyperspectral dataset. (a) The base LR hyperspectral image obtained by the Nuance NIR imaging spectrometer. (b) The HR color image obtained by a high-resolution digital camera, which was used as the reference data. (c) The ground truth selected manually to evaluate the classification result. (d) The classification result of (b) with SVM. (e) SASM. (f) SMMI. (g) MMSSM-L. (h) MMSSM-TV. (i) MMSSM-BTV.

multiple images, which provides more information about the distribution of the sub-pixels.

The quantitative indices lead to the same conclusion as the visual assessment. The accuracy of the different methods for the three simulated images is shown in Table III–V, in which the confusion matrix for the AVIRIS image was not given owing to the excessive classes. Generally speaking, the MAP-based multiple shifted images sub-pixel mapping (MMSSM) method shows a great improvement when compared with the traditional single image based sub-pixel mapping method, SASM, regardless of which prior model is used. For the Washington DC dataset, as shown in Table III, the MMSSM methods produce better results than the other two methods for all classes, especially the road class, as it was mainly confused by grass and tree because of the geographic proximity. Due to the complementary information of multiple shifted images being utilized to improve the accuracy of sub-pixel mapping, MMSSM exhibits excellent performance, compared with SASM. Generally speaking, MMSSM with the Laplacian prior (MMSSM-L) has the highest accuracy, and it improves the Kappa' coefficient

from 0.643 and 0.781 to 0.783, when compared with SASM and SMMI, a gain of 0.181 and 0.002, respectively. The reason for this is that the Laplacian prior denotes the high-pass operation with the constraint that the solution is smooth, which satisfies the spatial dependence assumption. The performance of MMSSM-TV is similar to MMSSM-L, owing to its ability to preserve the edges and detailed information in images, while MMSSM-BTV obtains the worst result, compared with the other two priors, because of its various parameters. Similarly, the same conclusion can be drawn for the Xiaqiao dataset. MMSSM with the Laplacian prior (MMSSM-L) and the TV prior (MMSSM-TV) obtain an approximate accuracy, and their accuracy is higher than that of MMSSM-BTV. As Table IV shows, the serious confusion which happens between grass and road was decreased greatly by MMSSM, which incorporates more of the information in multiple shifted images to help the solution of sub-pixel mapping. For the AVIRIS image, MMSSM-L obtains the highest accuracy as experiments of the other two images and a gain of 0.112 and 0.021 for Kappa' can be achieved comparing with SASM and SMMI respectively.

TABLE III
THE CONFUSION MATRIX STATISTICS (%) FOR THE WASHINGTON DC DATASET

Methods	Class	Water	Grass	Tree	Road
SASM	Water	96.07	0.06	0.50	2.75
	Grass	0.12	86.05	9.22	10.80
	Tree	0.99	9.16	85.99	12.34
	Road	2.82	4.73	4.29	74.10
SMMI	Water	97.67	0.48	0.85	2.07
	Grass	0.03	90.06	4.81	3.97
	Tree	0.90	7.33	92.15	8.54
	Road	1.41	2.13	2.20	85.42
MMSSM-L	Water	97.12	0.03	0.28	2.29
	Grass	0.02	91.87	5.75	5.37
	Tree	0.63	5.78	91.21	7.67
	Road	2.24	2.32	2.77	84.67
MMSSM-TV	Water	97.19	0.01	0.28	2.25
	Grass	0.03	91.83	5.76	5.42
	Tree	0.50	5.85	91.18	7.70
	Road	2.27	2.31	2.78	84.63
MMSSM-BTV	Water	96.99	0.01	0.32	2.36
	Grass	0.04	91.02	6.15	6.44
	Tree	0.70	6.23	90.32	8.74
	Road	2.26	2.74	3.21	82.45

According to the statistical accuracy, the MMSSM methods exhibit higher sub-pixel mapping accuracy than the traditional method which is based on a single image. Generally speaking, the performance of MMSSM methods is similar to the other multiple shifted images based method (SMMI) for both simulated images. However, the method with BTV prior is unsatisfactory owing to its various parameters. For the other two priors, the performance is slightly better than SMMI.

B. Experiment 2-Real Hyperspectral Image

To evaluate the application of sub-pixel mapping in practice, a real experiment was implemented by acquiring LR hyperspectral image sequences and a HR color image for the same area, simultaneously. The LR hyperspectral image sequences (50×50 pixels) used in this experiment were collected using the Nuance NIR imaging spectrometer. The acquired hyperspectral images have 46 bands, with spectral ranges from 650–1100 nm, and a 10 nm spectral interval. The HR color image (150×150) was obtained by a digital camera for the same scene. The scale factor

TABLE IV
THE CONFUSION MATRIX STATISTICS (%) FOR THE XIAQIAO DATASET

Methods	Class	Road	Water	Corn	Vegetable
SASM	Road	95.88	0.14	0.01	1.21
	Water	0.05	72.43	0.68	1.43
	Corn	0.00	13.65	96.51	7.65
	Vegetable	4.07	13.78	2.81	89.71
SMMI	Road	96.33	1.46	0.11	1.01
	Water	0.00	85.26	0.25	0.34
	Corn	0.00	8.61	97.79	2.30
	Vegetable	3.67	4.67	1.84	96.36
MMSSM-L	Road	98.25	0.27	0.00	0.49
	Water	0.05	85.68	0.43	0.52
	Corn	0.00	10.81	98.29	3.26
	Vegetable	1.69	3.24	1.28	95.72
MMSSM-TV	Road	98.20	0.27	0.00	0.51
	Water	0.05	85.41	0.43	0.56
	Corn	0.00	10.54	98.29	3.29
	Vegetable	1.75	3.78	1.28	95.64
MMSSM-BTV	Road	97.73	0.41	0.00	0.64
	Water	0.11	83.11	0.49	0.65
	Corn	0.00	11.89	98.00	3.91
	Vegetable	2.17	4.59	1.51	94.80

was three, and the number of LRF images was four in this experiment. One of the LR hyperspectral images was selected as the base image, and the registration of the base image and HR image was implemented by ENVI software. Then, all the LR hyperspectral images were unmixed to obtain the LRF images. The shifts of the other LRF images and the base LRF image were calculated with method proposed in [32] as previously described, and were (0.31, 0.13), (0.06, 0.15) and (−0.20, 0.56) respectively. The reference classification map was obtained by classifying the HR color image by SVM. Fig. 7(a)–(d) illustrates the base LR hyperspectral image, HR color image, ground truth, and the HR classification map, respectively. In this experiment, a new spectral unmixing method was utilized to obtain the LRF images, as described in [39]. As in [39], probabilistic support vector machine (P-SVM) was first utilized to determine if a pixel was pure by comparing the probability value with a chosen threshold. For those pixels with low probabilistic outputs, they were considered to be mixed pixels, and the fully constrained least squares (FCLS) method was applied to obtain the abundance.

TABLE V
THE ACCURACY OF SUB-PIXEL MAPPING IN THE SIMULATED EXPERIMENTS

Accuracy		Single image based sub-pixel mapping	Multiple shifted images based sub-pixel mapping			
		SASM	SMMI	MMSSM -L	MMSSM -TV	MMSSM -BTV
Washington DC	PCC	85.85%	91.25%	91.41%	91.39%	90.46%
	Kappa	0.799	0.876	0.878	0.878	0.865
	PCC'	75.83%	85.13%	85.32%	85.29%	83.70%
	Kappa'	0.643	0.781	0.783	0.783	0.759
Xiaqiao	PCC	94.10%	96.96%	97.29%	97.26%	96.76%
	Kappa	0.884	0.941	0.947	0.946	0.936
	PCC'	82.70%	91.36%	92.07%	91.98%	90.51%
	Kappa'	0.721	0.859	0.872	0.870	0.847
Indian Pines	PCC	93.89%	96.57%	97.40%	97.25%	96.30%
	Kappa	0.919	0.955	0.965	0.963	0.951
	PCC'	84.26%	91.64%	93.30%	92.93%	90.46%
	Kappa'	0.804	0.895	0.916	0.912	0.881

TABLE VI
THE ACCURACY OF THE CLASSIFICATION METHOD FOR THE NUANCE IMAGE

Methods	Class	Withered vegetable	Fresh vegetable	Background
SVM	Withered vegetable	2012	0	0
	Fresh vegetable	1	731	2
	Background	0	25	1087
PCC = 99.27% Kappa = 0.988				

After the LRF images were obtained, the proposed method was used to perform the task of sub-pixel mapping. Three major land-cover classes can be distinguished in this experiment: withered vegetable, fresh vegetable, and the black paper, which was used as the background. Fig. 7(e), (f) and (g)–(i) illustrates the sub-pixel mapping results using SASM, SMMI, and the proposed method, respectively.

The classification accuracies are listed in Table VI. The results show that misclassification occurs between fresh vegetable and the background, owing to the geographic proximity. With an accuracy of 0.988, this classification result can be used as the reference data in this experiment.

Unlike the simulated experiments, more error sources were introduced in the real experiment, including the classification error of the HR color image, the unmixing error of the LR hyperspectral images, the error of the sub-pixel mapping method, the registration errors between the LRF images, and the registration error of the base LR hyperspectral image and the HR color

image. Compared with the reference classification map, the results of SASM are seriously affected by the error of spectral unmixing, while that of the proposed method is more smooth, due to the integration of the information of multiple shifted images. The proposed method can provide a better visual result; however, it is sensitive to spectral unmixing and the accuracy of registration between LRF images, as some details may be eliminated due to the unmixing error and excessive smoothing. There is a trade-off between smoothing and detail preservation, in that smoothing can restrain the error of spectral unmixing while eliminating the potential tiny features.

The sub-pixel mapping accuracies are listed in Tables VII and VIII to evaluate the effectiveness of the proposed method. Due to the inaccuracy of spectral unmixing, only PCC and the Kappa coefficient were considered in the real experiment. Gains of 5.56%, 5.54% and 5.09% for PCC over SASM were obtained for the proposed method, with the different priors, respectively. MMSSM-L obtained the best accuracy, and MMSSM-BTV had the worst performance, for the same reasons as the simulated experiment. The confusion matrix in Table VII reveals that the MMSSM methods have a better result than SASM in all classes, and the greatest confusion is between background and fresh vegetation, because they are seriously mixed in this image. Unlike the simulated images, the SMMI performs poor when it comes to real experiment, the accuracy of which is even worse than SASM because it's sensitive to the accuracy of image registration. With accurate shifts, the SMMI can obtain approximate accuracy with proposed method as simulated experiments illustrate. However, the proposed method is more robust when the image registration parameters are not accurate. The accuracies indicate that the proposed method is an effective way to improve

TABLE VII
THE CONFUSION MATRIX STATISTICS (%) FOR THE NUANCE DATASET

Methods	Class	Withered vegetable	Fresh vegetable	Background
SASM	Withered vegetable	89.78	16.36	5.62
	Fresh vegetable	6.62	66.82	35.38
	Background	3.59	16.83	59.00
SMMI	Withered vegetable	71.52	0.96	0.20
	Fresh vegetable	10.26	38.84	3.46
	Background	18.22	60.19	96.34
MMSSM-L	Withered vegetable	92.07	10.86	1.15
	Fresh vegetable	5.23	70.22	27.12
	Background	2.70	18.92	71.73
MMSSM-TV	Withered vegetable	91.57	10.55	1.10
	Fresh vegetable	5.57	70.71	27.49
	Background	2.87	18.73	71.42
MMSSM-BTV	Withered vegetable	90.70	10.38	1.06
	Fresh vegetable	6.09	70.10	27.24
	Background	3.21	19.52	71.70

TABLE VIII
THE ACCURACY OF SUB-PIXEL MAPPING IN THE REAL EXPERIMENT

Accuracy	Single image based sub-pixel mapping	Multiple shifted images based sub-pixel mapping			
	SASM	SMMI	MMSSM-L	MMSSM-TV	MMSSM-BTV
PCC	71.60%	63.99%	77.16%	77.14%	76.69%
Kappa	0.566	0.479	0.653	0.652	0.645

the performance of sub-pixel mapping, compared with the two other methods.

C. Parameter Analysis

1) *Impact of the Regularization Parameter:* In the MAP model presented in (10), the regularization parameter λ plays a very important role, in that it controls the relative contribution between the data fidelity and prior item. If the value selected is too small, the noise will not be well suppressed; inversely, if the value selected is too large, the result will be blurred [33]. To show the robustness of the proposed method with regard to the regularization parameter λ , we plotted the curve of the PCC value with different values of the parameter λ for the three priors in the simulated Washington DC dataset and the Nuance dataset, as shown in Fig. 8(a), (b). Fig. 8 shows that the performance of the proposed method with different priors is not consistent for the same regularization parameter. The Laplacian prior model can obtain the best accuracy when the value of λ is small; how-

ever, the accuracy decreases greatly if λ exceeds a certain numerical value. For the TV and BTV prior models, the change in accuracy is slower than the Laplacian prior model when λ increases. That is, they are more stable than the Laplacian prior model. Generally speaking, the change of λ has a very large effect on the results of the Laplacian prior model, although it obtains the best accuracy. The TV and BTV prior models are robust with regard to changes of the parameter λ , and the PCC value remains little changed when λ is set to be a large value. In addition, the optimal accuracy of the TV prior is more or less the same as that of the Laplacian prior, while that of BTV is a little lower than the other two priors.

2) *Impact of Image Registration:* The image registration is very important procedure in this proposed method. For the real experiment, the approximate shifts of LRF images were calculated by method proposed in [32]. However, the impact of imager registration should be discussed because different combinations of shifts may have a great influence on the sub-pixel

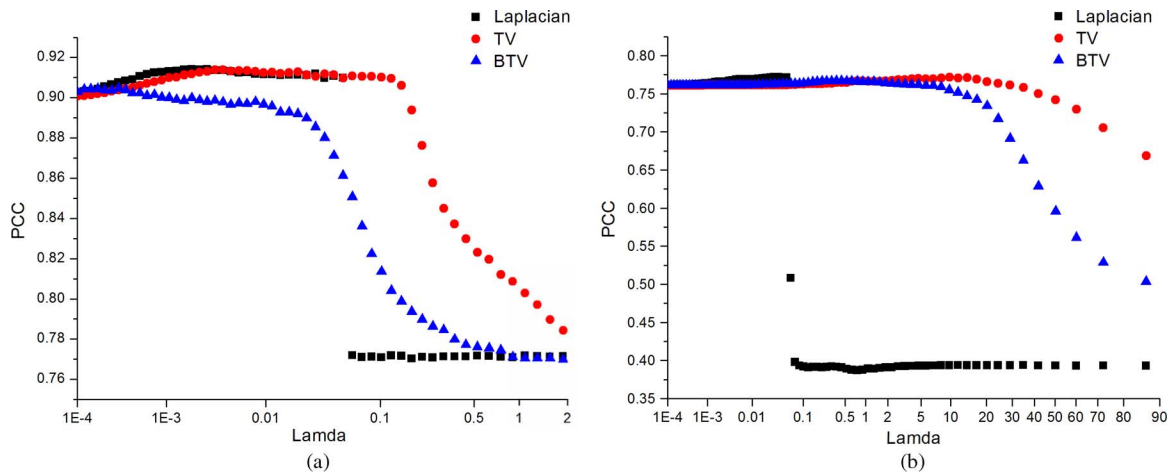


Fig. 8. A comparison of the performance of the proposed method with different priors and regularization parameters for both experiments. (a) Simulated experiment with the Washington DC dataset. (b) Real experiment with the Nuance dataset.

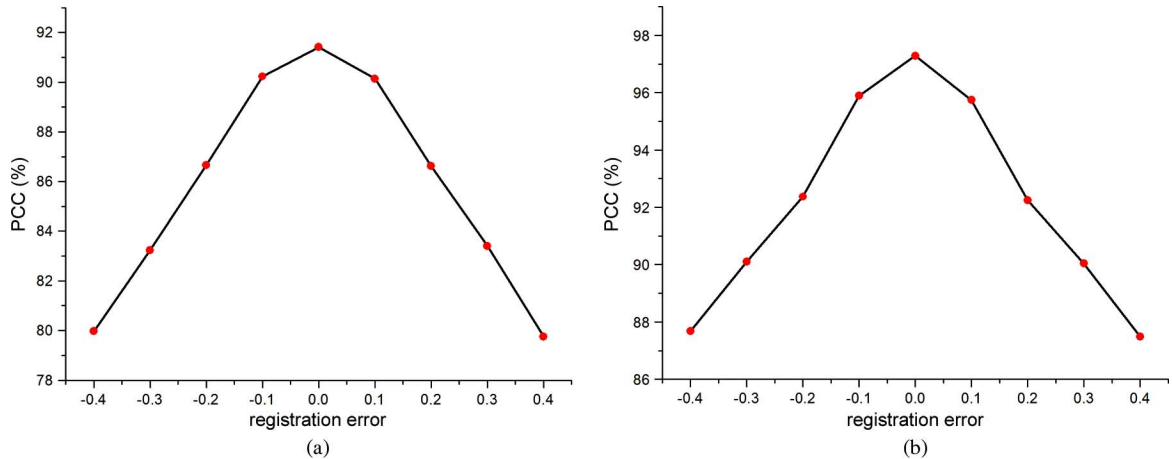


Fig. 9. A comparison of the performance of the proposed method given different registration errors for the simulated experiments. (a) The result with the Washington DC dataset. (b) The result with the Xiaqiao image.

mapping result. In this section, two simulated images were used to evaluate the impact of registration error. The accurate combination of shifts used in this experiment is $(-0.5, 0)$, $(0.5, 0)$, $(0, -0.5)$, $(0, 0.5)$ for the four auxiliary images. To evaluate the impact of different combinations of shifts, the registration error was used to adjust the shifts. If the registration error is equal to 0.1, the combination of shifts used is $(-0.4, 0.1)$, $(0.6, 0.1)$, $(0.1, -0.4)$, $(0.1, 0.6)$. Fig. 9 illustrates the accuracy of proposed method with Laplacian prior given different registration errors for both simulated images. When the combination of shifts is accurate, which means the registration error is 0, the proposed method obtains the highest accuracy. As the absolute value of registration error improves, the accuracy decreases greatly.

V. EXPERIMENTS AND ANALYSIS

A sub-pixel mapping framework based on a MAP model with multiple shifted hyperspectral images, namely MMSSM, is proposed to utilize the complementary information in images which have sub-pixel shifts, in order to improve the performance of sub-pixel mapping. Traditional sub-pixel mapping methods are based on a single image, which is inadequate because of the

lack of information. A type of auxiliary data that can provide more details at the sub-pixel level is multiple shifted images acquired for the same area, with sub-pixel shifts. MMSSM utilizes a MAP model, which has the ability to regularize the ill-posed problem by adding prior information in order to convert the data to a better sub-pixel mapping result. In MMSSM, LRF images for all the low-resolution hyperspectral images are first obtained by spectral unmixing, and the sub-pixel shifts between the LRF images are precisely calculated. Based on the LRF images, the MAP model incorporates the image information of the same land-cover class to obtain a resolution-enhanced map. The spatial distribution of the different classes can be determined by integrating these resolution-enhanced maps. Three prior models (Laplacian, TV and BTV), which are used in MMSSM to regularize the sub-pixel mapping problem, were introduced to verify the performance of the proposed method for sub-pixel mapping. Compared with traditional single image based method, experimental results using both synthetic and real multiple shifted hyperspectral images indicated that MMSSM is an efficient sub-pixel mapping technique for improving accuracy and visual assessment. An analysis of the λ parameter and the image registration is also provided. Future research will focus on further

improvements of the proposed techniques, such as the adaptive selection of the regularization parameter.

ACKNOWLEDGMENT

The authors would like to thank the editor, associate editor and anonymous reviewers for their helpful comments and suggestions, Dr. F. Ling of the Institute of Geodesy and Geophysics, Chinese Academy of Sciences for providing the code of their algorithm, and also the research group supervised by Prof. D. Landgrebe, Purdue University, West Lafayette, IN, for providing the free downloads of the AVIRIS Image.

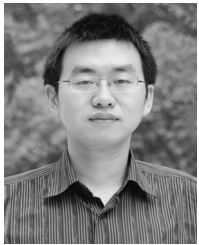
REFERENCES

- [1] G. M. Foody, "Hard and soft classifications by a neural network with a non-exhaustively defined set of classes," *Int. J. Remote Sens.*, vol. 23, no. 18, pp. 3853–3864, Jan. 2002.
- [2] L. Zhang, B. Wu, B. Huang, and P. Li, "Nonlinear estimation of subpixel proportion via kernel least square regression," *Int. J. Remote Sens.*, vol. 28, no. 18, pp. 4157–4172, Sept. 2007.
- [3] P. M. Atkinson, "Mapping sub-pixel boundaries from remotely sensed images," in *Innovations in GIS IV*. London, U.K.: Taylor and Francis, 1997, ch. 12, pp. 166–180.
- [4] A. J. Tatem, H. G. Lewis, P. M. Atkinson, and M. S. Nixon, "Super-resolution target identification from remotely sensed images using a Hopfield neural network," *IEEE Trans. Geosci. Remote Sens.*, vol. 39, no. 4, pp. 781–796, Apr. 2001.
- [5] A. J. Tatem, H. G. Lewis, P. M. Atkinson, and M. S. Nixon, "Multiple-class land-cover mapping at the sub-pixel scale using a Hopfield neural network," *Int. J. Appl. Earth Obs. Geoinf.*, vol. 3, no. 2, pp. 184–190, 2001.
- [6] A. J. Tatem, H. G. Lewis, P. M. Atkinson, and M. S. Nixon, "Super-resolution land cover pattern prediction using a Hopfield neural network," *Remote Sens. Environ.*, vol. 79, no. 1, pp. 1–14, Jan. 2002.
- [7] Y. Su, G. Foody, A. Muad, and K. Cheng, "Combining Hopfield neural network and contouring methods to enhance super-resolution mapping," *IEEE J. Sel. Topics Appl. Earth Observ. Remote Sens. (JSTARS)*, vol. 5, no. 5, 2012.
- [8] K. C. Mertens, L. P. C. Verbeke, T. Westra, and R. R. D. Wulf, "Sub-pixel mapping and sub-pixel sharpening using neural network predicted wavelet coefficients," *Remote Sens. Environ.*, vol. 91, no. 2, pp. 225–236, May 2004.
- [9] L. Zhang, K. Wu, Y. Zhong, and P. Li, "A new sub-pixel mapping algorithm based on a BP neural network with an observation model," *Neurocomputing*, vol. 71, no. 10–12, pp. 2046–2054, Jun. 2008.
- [10] J. Verhoeve and R. R. D. Wulf, "Land cover mapping at sub-pixel scales using linear optimization techniques," *Remote Sens. Environ.*, vol. 79, no. 1, pp. 96–104, Jan. 2002.
- [11] K. C. Mertens, B. D. Baets, L. P. C. Verbeke, and R. R. D. Wulf, "A sub-pixel mapping algorithm based on sub-pixel/pixel spatial attraction models," *Int. J. Remote Sens.*, vol. 27, no. 15, pp. 3293–3310, Aug. 2006.
- [12] P. M. Atkinson, "Sub-pixel target mapping from soft-classified, remotely sensed imagery," *Photogramm. Eng. Remote Sens.*, vol. 71, no. 7, pp. 839–846, Jul. 2005.
- [13] K. C. Mertens, L. P. C. Verbeke, E. I. Ducheyne, and R. R. D. Wulf, "Using genetic algorithms in sub-pixel mapping," *Int. J. Remote Sens.*, vol. 24, no. 21, pp. 4241–4247, Nov. 2003.
- [14] Y. Zhong, L. Zhang, P. Li, and H. Shen, "A sub-pixel mapping algorithm based on artificial immune systems for remote sensing imagery," in *Geoscience and Remote Sensing Symp., 2009 IEEE Int., IGARSS 2009*, pp. III-1007–III-1010.
- [15] T. Kasetkasem, M. K. Arora, and P. K. Varshney, "Super-resolution land cover mapping using a Markov random field based approach," *Remote Sens. Environ.*, vol. 96, no. 3/4, pp. 302–314, Jun. 2005.
- [16] V. A. Tolpekin and A. Stein, "Quantification of the effects of land-cover-class spectral separability on the accuracy of markov-random-field-based superresolution Mapping," *IEEE Trans. Geosci. Remote Sens.*, vol. 47, no. 9, pp. 3283–3297, Sept. 2009.
- [17] Y. Shao and R. S. Lunetta, "Sub-pixel mapping of tree canopy, impervious surfaces, and cropland in the laurentian great lakes basin using MODIS time-series data," *IEEE J. Sel. Topics Appl. Earth Observ. Remote Sens. (JSTARS)*, vol. 4, no. 2, Jun. 2011.
- [18] Q. M. Nguyen, P. M. Atkinson, and H. G. Lewis, "Super resolution mapping using a Hopfield neural network with fused images," *IEEE Trans. Geosci. Remote Sens.*, vol. 44, pp. 736–749, Mar. 2006.
- [19] F. Ling, Y. Du, F. Xiao, H. Xue, and S. Wu, "Super-resolution land-cover mapping using multiple sub-pixel shifted remotely sensed images," *Int. J. Remote Sens.*, vol. 31, no. 19, pp. 5023–5040, Oct. 2010.
- [20] Q. M. Nguyen, P. M. Atkinson, and H. G. Lewis, "Super-resolution mapping using Hopfield neural network with LIDAR data," *IEEE Geosci. Remote Sens. Lett.*, vol. 2, no. 3, pp. 366–370, Jul. 2005.
- [21] Q. M. Nguyen, P. M. Atkinson, and H. G. Lewis, "Super-resolution mapping using Hopfield Neural Network with panchromatic imagery," *Int. J. Remote Sens.*, vol. 32, no. 21, pp. 6149–6177, Jul. 2011.
- [22] T. S. Huang and R. Y. Tsai, "Multi-frame image restoration and registration," *Adv. Comput. Vis. Image Process.*, vol. 1, pp. 317–339, 1984.
- [23] S. Park, M. Park, and M. G. Kang, "Super-resolution image reconstruction, a technical overview," *IEEE Signal Process. Mag.*, vol. 20, no. 5, pp. 21–36, May 2003.
- [24] R. R. Schultz and R. L. Stevenson, "Extraction of high-resolution frames from video sequences," *IEEE Trans. Image Process.*, vol. 5, no. 6, pp. 996–1011, 1996.
- [25] L. C. Pickup, D. P. Capel, S. J. Roberts, and A. Zisserman, "Bayesian image super-resolution, continued," *Adv. Neur. In.*, vol. 19, pp. 1089–1096, 2006.
- [26] J. Ma, J. C. C. Wai, and F. Canters, "An operational superresolution approach for multi-temporal and multi-angle remotely sensed imagery," *IEEE J. Sel. Topics Appl. Earth Observ. Remote Sens. (JSTARS)*, vol. 5, no. 1, pp. 110–124, Feb. 2012.
- [27] E. S. Lee and M. G. Kang, "Regularized adaptive high-resolution image reconstruction considering inaccurate subpixel registration," *IEEE Trans. Image Process.*, vol. 12, no. 7, pp. 826–837, Jul. 2003.
- [28] M. Ng, H. Shen, E. Lam, and L. Zhang, "A total variation regularization based super resolution reconstruction algorithm for digital video," *EURASIP J. Adv. Signal Process.*, pp. 1–16, 2007, Article ID 74585.
- [29] S. Farsiu, M. Robinson, M. Elad, and P. Milanfar, "Fast and robust multiframe super-resolution," *IEEE Trans. Image Process.*, vol. 13, no. 10, pp. 1327–1344, 2004.
- [30] P. Fisher, "The pixel: A snare and a delusion," *Int. J. Remote Sens.*, vol. 18, no. 3, pp. 679–685, Feb. 1997.
- [31] S. Borman and R. L. Stevenson, Spatial Resolution Enhancement of Low-Resolution Image Sequences. A Comprehensive Review With Directions for Future Research Lab. Image and Signal Analysis, University of Notre Dame, 1998, Tech. Rep..
- [32] L. Zhang, H. Zhang, H. Shen, and P. Li, "A super-resolution reconstruction algorithm for surveillance images," *Signal Process.*, vol. 90, no. 3, pp. 848–859, 2010.
- [33] Q. Yuan, L. Zhang, H. Shen, and P. Li, "Adaptive multiple-frame image super-resolution based on U-curve," *IEEE Trans. Image Process.*, vol. 19, no. 12, pp. 3157–3170, Dec. 2010.
- [34] A. Kanemura, S. Maeda, and S. Ishii, "Superresolution with compound Markov random fields via the variational EM algorithm," *Neural Netw.*, vol. 22, no. 7, pp. 1025–1034, 2009.
- [35] Y. Li, D. Dai, and L. Shen, "Multiframe super-resolution reconstruction using sparse directional regularization," *IEEE Trans. Circuits Syst. Video Technol.*, vol. 20, no. 7, pp. 945–956, 2010.
- [36] H. Shen, L. Zhang, B. Huang, and P. Li, "A MAP approach for joint motion estimation, segmentation and super-resolution," *IEEE Trans. Image Process.*, vol. 16, no. 2, pp. 479–490, Feb. 2007.
- [37] D. Landgrebe, *Signal Theory Methods in Multispectral Remote Sensing*. New Jersey, USA: Wiley, 2003.
- [38] American ITT Visual Information Solutions Company, ENVI Online Tutorials [EB/OL] [Online]. Available: <http://www.itvis.com/ProductServices/ENVI.aspx>
- [39] A. Villa, J. Chanussot, J. A. Benediktsson, and C. Jutten, "Spectral unmixing for the classification of hyperspectral images at a finer spatial resolution," *IEEE J. Sel. Topics Signal Process.*, vol. 5, no. 3, pp. 521–533, Jun. 2011.



Xiong Xu received the B.S. degree in photogrammetry from Wuhan University, Wuhan, China, in 2008, where he is currently working toward the Ph.D. degree in photogrammetry and remote sensing in the State Key Laboratory of Information Engineering in Surveying, Mapping, and Remote Sensing at Wuhan University, Wuhan.

His research interests include multi- and hyper-spectral image processing, artificial neural network, and pattern recognition.



Yanfei Zhong (M'11) received the B.S. degree in information engineering and the Ph.D. degree in photogrammetry and remote sensing from Wuhan University, China, in 2002 and 2007, respectively.

He has been with the State Key Laboratory of Information Engineering in Surveying, Mapping and Remote Sensing, Wuhan University since 2007 and is currently a Professor. His research interests include multi- and hyperspectral remote sensing image processing, artificial intelligence, and pattern recognition. He has published more than ten peer-reviewed articles in international journals such as IEEE TRANSACTIONS ON GEOSCIENCE AND REMOTE SENSING and IEEE TRANSACTIONS ON SYSTEMS, MAN AND CYBERNETICS, PART B.

Dr. Zhong was the recipient of the National Excellent Doctoral Dissertation Award of China (2009) and New Century Excellent Talents in University of China (2009). He was a Referee of IEEE TRANSACTIONS ON SYSTEMS, MAN AND CYBERNETICS, PART B, IEEE JOURNAL OF SELECTED TOPICS IN APPLIED EARTH OBSERVATIONS AND REMOTE SENSING, and *Pattern Recognition*.

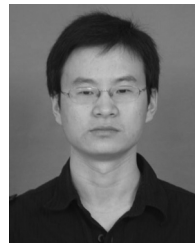
Dr. Zhong was the recipient of the National Excellent Doctoral Dissertation Award of China (2009) and New Century Excellent Talents in University of China (2009). He was a Referee of IEEE TRANSACTIONS ON SYSTEMS, MAN AND CYBERNETICS, PART B, IEEE JOURNAL OF SELECTED TOPICS IN APPLIED EARTH OBSERVATIONS AND REMOTE SENSING, and *Pattern Recognition*.



Liangpei Zhang (M'06–SM'08) received the B.S. degree in physics from Hunan Normal University, ChangSha, China, in 1982, the M.S. degree in optics from the Xi'an Institute of Optics and Precision Mechanics of Chinese Academy of Sciences, Xi'an, China, in 1988, and the Ph.D. degree in Photogrammetry and Remote Sensing from Wuhan University, Wuhan, China, in 1998.

He is currently with the State Key Laboratory of Information Engineering in Surveying, Mapping and Remote Sensing, Wuhan University, as the head of the Remote Sensing Division. He is also a "Chang-Jiang Scholar" Chair Professor appointed by the Ministry of Education, China. He is currently the Principal Scientist for the China State Key Basic Research Project (2011–2016) appointed by the Ministry of National Science and Technology of China to lead the remote sensing program in China. He is an Executive Member (Board of Governor) of the China National Committee of International Geosphere-Biosphere Programme. He also serves as an Associate Editor of International Journal of Ambient Computing and Intelligence, International Journal of Image and Graphics, International Journal of Digital Multimedia Broadcasting, Journal of Geo-spatial Information Science, and the Journal of Remote Sensing. He has more than 260 research papers and is the holder of five patents. His research interests include hyperspectral remote sensing, high resolution remote sensing, image processing and artificial intelligence.

Dr. Zhang is a Fellow of the Institution of Electrical Engineers, an executive Member for the China Society of Image and Graphics, and others. He regularly serves as a Cochair of the series SPIE Conferences on Multispectral Image Processing and Pattern Recognition, Conference on Asia Remote Sensing, and many other conferences. He edits several conference proceedings, issues, and the Geoinformatics Symposiums.



Hongyan Zhang received the B.S. degree in geographic information system and the Ph.D. degree in photogrammetry and remote sensing from Wuhan University, Wuhan, China, in 2005 and 2010, respectively.

Since 2010, he has been a Lecturer with the State Key Laboratory of Information Engineering in Surveying, Mapping, and Remote Sensing, Wuhan University. His current research interests focus on image reconstruction and remote sensing image processing.